ChemBioChem

Chemistry Europe
European Chemical Societies Publishing
ChemBioChem

RESEARCH ARTICLE OPEN ACCESS

Heterocyclic-Fused Squaramides: Anionophores With Antimicrobial Activity

Luke Edward Brennan[1,2,3] | Chris Samuel Hawes[4] | Kevin Kavanagh[2,5,6] | Robert Brian Peter Elmes[1,2,6]

[1]Department of Chemistry, Maynooth University, Maynooth, Ireland | [2]Synthesis and Solid State Pharmaceutical Centre (SSPC), Maynooth University, Maynooth, Ireland | [3]Department of Chemistry, Royal College of Surgeons in Ireland, Dublin 2, Ireland | [4]School of Chemical and Physical Sciences, Keele University, Keele, UK | [5]Department of Biology, Maynooth University, Maynooth, Ireland | [6]Kathleen Lonsdale Institute for Human Health Research, Maynooth University, Maynooth, Ireland

Correspondence: Robert Brian Peter Elmes (robert.elmes@mu.ie)

Received: 11 November 2025 | **Revised:** 14 January 2026 | **Accepted:** 14 January 2026

Keywords: anion transport | antimicrobial resistance | chemical biology | squaramides | supramolecular chemistry

ABSTRACT

Antimicrobial resistance is regarded as one of the foremost public health risks of the 21st century, highlighting the need for new antimicrobial agents and chemical tools to interrogate their biological activity. Artificial transmembrane anion transporters have emerged as promising supramolecular scaffolds in this context, having demonstrated membrane activity in mammalian systems and showing growing potential in antimicrobial research. Here, we report a series of heterocycle-fused squaramide anionophores capable of binding and transporting chloride. Several members of this series display measurable antimicrobial activity, alongside evidence of intracellular chloride modulation in bacterial cells. Taken together, these findings indicate that membrane localisation and anion transport are important contributing factors to the observed antimicrobial effects, and support further investigation of squaramide-based anionophores as membrane-active chemical biology tools.

1 | Introduction

Antimicrobial resistance (AMR) is often referred to as a silent pandemic, and is one of the most serious threats to medicine in the modern age [1]. Indeed, AMR is expected to cause upward of 10 million deaths annually, by 2050 [2]. With constantly emerging mechanisms of resistance, and the paucity of novel drugs, there is an urgent need for antimicrobial drugs that exhibit a distinct mechanism of action (MOA) than those currently in circulation [1, 3–8].

Since the advent of host–guest chemistry in the 1960s [9–11], there has been increased interest in the medicinal chemistry of supramolecular systems, most notably in the use of anion transport to develop novel therapeutics [12–14]. Anionophores have seen applications in the medicinal chemistry space, from their use in the development of therapeutics for cystic fibrosis [14, 15], to disruptors of anion homeostasis in-cellulo [16]. Considerable effort has been made towards the development of anionophores that exhibit interesting biological activity [14, 17, 18]. This focus on the medicinal chemistry of transporters has given rise to examples of active compounds such as squaramides that disrupt autophagy through alteration of lysosomal pH [19], to 1,8-naphthalimide-urea conjugates with potent cytotoxicity [20], and numerous tambjamine-like alkaloids that exhibit anticancer activity [21]. Despite the utility of supramolecular chemistry in the development of novel therapeutics, there has been little focus on the use of synthetic anion transporters in the development of novel antimicrobials—[22–25] a surprising fact considering the antimicrobial activity of cationophores such as monensin, salinomycin, valinomycin, and lasalocid is well established [26]. However, while recent reports of compounds demonstrating antimicrobial activity have also displayed anion transport behaviour, the link between anionophorism and antimicrobial effect was not directly correlated. Recently, Busschaert and co-workers reported a urea-based anion transporter, that exhibits high levels of antimicrobial activity. In an effort to

elucidate the MOA, bacterial cytological profiling was employed as a high throughput method and concluded that the antimicrobial activity was most likely as a result of anion transport—a major step towards rational design of antimicrobial anionophores [27]. Following this, our group reported the synthesis of a series of four non-toxic 'Squindoles' that demonstrated potent anion transport through CH—NH bonding and high levels of antimicrobial activity against *Staphylococcus aureus* (SA) and methicillin-resistant *Staphylococcus aureus* (MRSA), even evading resistance over multiple generations. Furthermore, using a combination of chemical biology tools, this work verified the link between anion transport and antimicrobial activity [28]. Most recently, we have deduced through a combination of spectroscopic techniques, and cellular assays that a series of adamantylsquaramide derivatives display potent antimicrobial activity through both anion transport and membrane disruption [29]. In the present study, heterocyclic-fused squaramides were selected as a modular platform to systematically vary heterocycle identity, π-surface extension, and electronic character while retaining a conserved squaramide anion-binding motif, enabling exploration of how these parameters influence membrane localisation, anion transport behaviour, and antimicrobial activity.

Herein, we build upon our recent results and explore an expanded chemical space of heterocyclic-fused squaramides through the design and synthesis of compounds **1–8** (Figure 1). Selected compounds exhibit antimicrobial activity against MRSA and show the capacity to modulate intracellular chloride concentrations in bacterial cells. Furthermore, using super-resolution nanoscopy, we confirm membrane localisation of these compounds, supporting the view that membrane interaction and anion transport are important contributing factors to their observed antimicrobial activity.

2 | Results and Discussion

2.1 | Receptor Synthesis

1–8 were accessed through the synthetic approach outlined in Scheme 1, whereby, the synthesis diverges in steps toward an *N*-Phenyl derivative of the respective subclass. Initially, diethyl squarate, **S1**, the relevant cyclobutene *ortho*-ethoxy ester utilised in the synthesis of squaramides was synthesised as outlined previously [30]. The three relevant heterocyclic squarate esters, **S2–S4** were accessed through conjugate addition of previously *N*-alkylated heterocycles (**A1–A3**), under basic conditions to afford the desired squarates in 35%–53% yield, following flash column chromatography.

S1–S3 were subsequently reacted with either 3,5-bis(trifluoromethyl)aniline, or 4-trifluoromethylaniline under Lewis acidic conditions, to afford the desired squaramides in 6%–69% yield, depending on the electronic contributions of the aniline, and the squarate used. The successful synthesis of each compound was confirmed by ^{1}H, ^{13}C NMR spectroscopy, and high-resolution mass spectrometry (HRMS), and all experimental details can be found in the ESI. In the case of compound **1** we were also able to successfully obtain an X-ray crystal structure as a DMSO solvate (See ESI). Through recrystallisation from a supersaturated solution of **1** in DMSO, we confirmed the desired *cis*-conformation around the double bond as had been previously

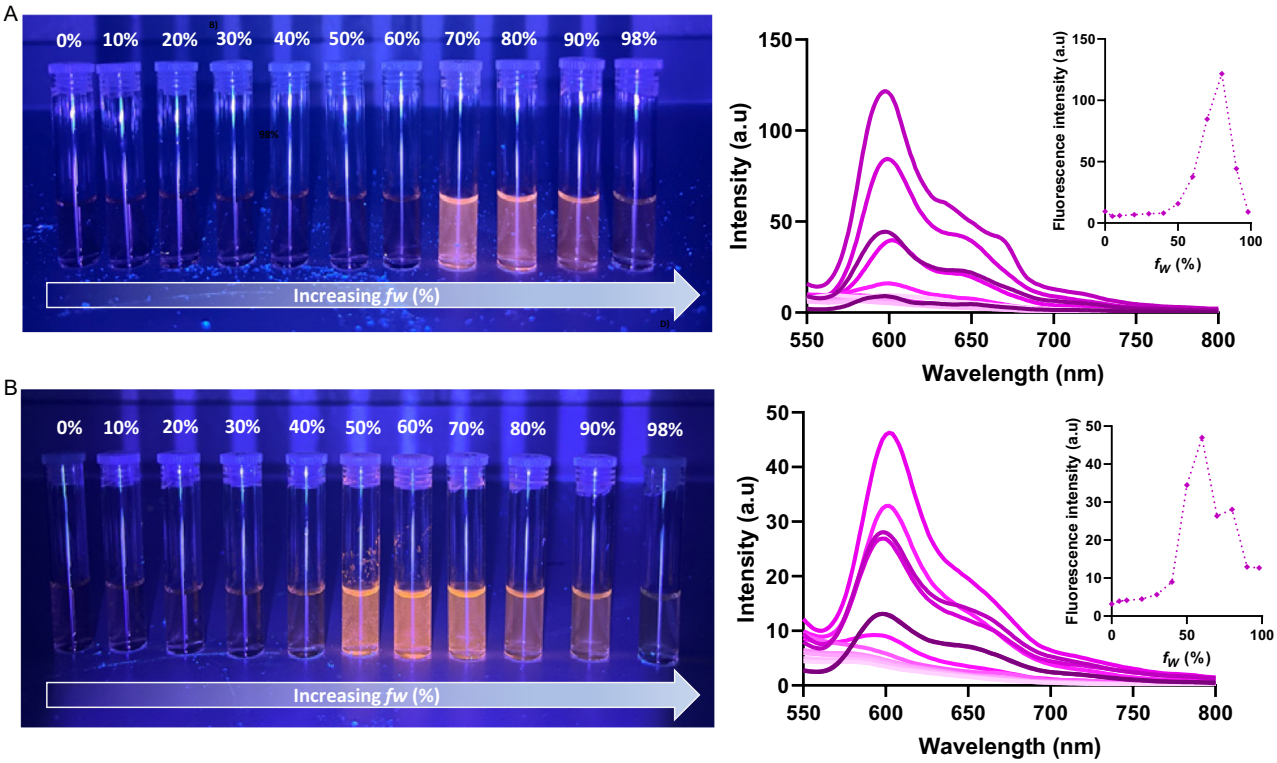

FIGURE 1 | Visual and spectroscopic determination of the AIE properties of **3** and **4**. (A) UV visualisation of the impact of increasing f_w (0%–98% H_2O) in aqueous THF mixtures containing **3** (20 μM), and spectroscopic study of AIE under the same conditions. (B) UV visualisation of the impact of increasing f_w (0%–98% H_2O) in aqueous THF mixtures containing **4** (20 μM), and spectroscopic study of AIE under the same conditions (light to dark pink infers increasing f_w).

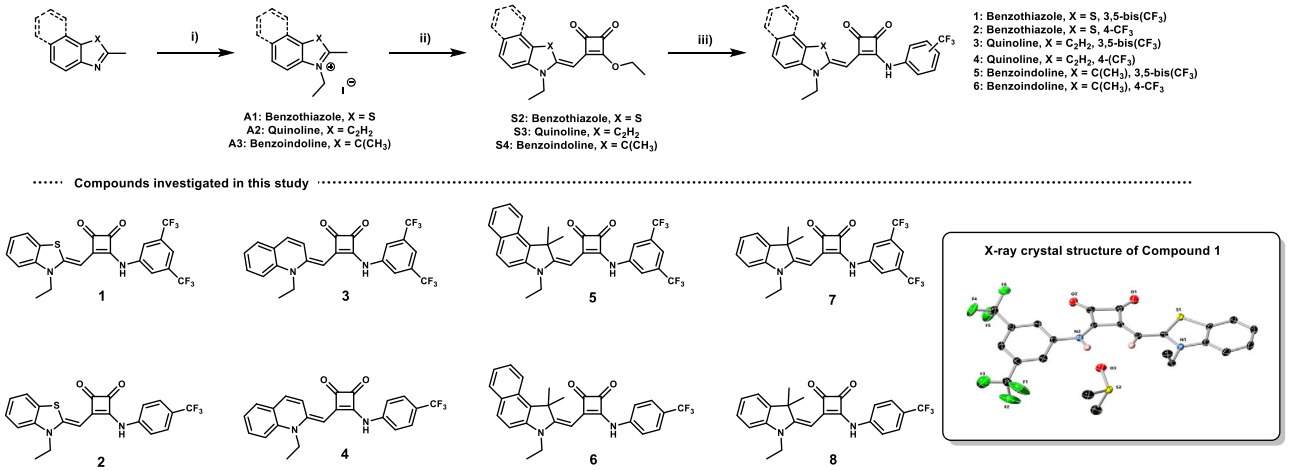

SCHEME 1 | The synthesis of heterocyclic squaramides 1–8. Reagents and conditions: (i) Ethyl iodide, MeCN, reflux, 18 h, 54%–70%; (ii) TEA, EtOH, N_2, reflux, 3–18 h, 35%–53%; (iii) aromatic amine, $Zn(OTf)_2$, EtOH, reflux, 6%–69%. **Inset**: X-ray crystal structure of Compound **1** as the DMSO solvate.

observed for **7** and **8**—an important factor in their anion recognition ability.

Analysis of the yellow block crystals of **1** by single crystal X-ray diffraction provided a structural model in the monoclinic space group *P*21/*c*, where the asymmetric unit contains one molecule of the title compound as the DMSO solvate (Scheme 1;Inset). The molecule adopts a relatively planar conformation with the benzothiazole ring oriented in a *syn* coplanar orientation relative to the squaramide core, evidenced by the torsion angle S1-C9-C10-C11 of 3.7(6)°. In this conformation, the S···O distance between the benzothiazole sulphur atom and the nearby ketone oxygen atom O1 of 3.039(3) Å is similar to those seen in weak intramolecular chalcogen bonds [31], although the C═O···S angle of 94.3(2)° most likely limits any potential stabilisation from this close contact. Conversely, a slight rotation is observed for the bis-trifluoromethylphenyl substituent, which adopts a C16-C15-N2-C14 torsion angle of −20.3(6)°. The benzothiazoline group itself forms a non-symmetric hydrogen bonding chelate with the lattice DMSO molecule; the N─H group forms the stronger of the two contacts at an N1···O3 distance of 2.864(4) Å, compared to the much longer C10···O3 distance of 3.363(4) Å. Beyond these interactions, the remaining intermolecular contacts in the structure of **1** are mostly accounted by a parallel head-to-tail $\pi\cdots\pi$ interaction across the aromatic surface of the molecule. The two molecules are separated by a mean interplanar distance of 3.42 Å, and this contact is buttressed by a weak C─H···O contact from the lattice DMSO molecule to the ketone oxygen atom O1 at a C···O distance of 3.289(5) Å.

2.2 | Physiochemical and Photophysical Properties

With the knowledge that compounds **7** and **8** exhibit bright green fluorescence, we sought to determine how the incorporation of varying heterocycles influenced the absorption and emission properties of each compound. Spectrophotometric determination of the λ_{max} (abs/em) was performed in DMSO at a concentration of 10 μM. Values for λ_{max} (abs/em), and stokes shift are tabulated below (Table 1), and represented visually as normalised excitation/emission spectra for each compound (see ESI).

TABLE 1 | Summary of the λ_{max} (abs/em), and stokes shift ($\Delta\lambda$) for compounds 1–8, determined from a 10 μM solution of each in DMSO (or H_2O:DMSO (70:30) for 3 and 4.

Compound	λ_{max} (abs), nm	λmax (em), nm	Δλ, nm
1	465	489	24
2	466	489	23
3	495	602	107
4	494	605	111
5	455	498	43
6	458	503	45
7[a]	450	490	40
8[a]	450	490	40

[a]Data taken from Ref. [16].

From our initial spectroscopic study, we determined that the innate emissive properties of each compound are greatly influenced by the heterocyclic framework employed. In the case of **1**, **2**, **5**, and **6** we observed bright emission centred ca. 490 nm for each. Interestingly, **3** and **4** appeared to display little to no observable fluorescence, which we suspected may be a result of the non-restricted rotation around the olefinic C─C bond observed in each. When compared to both benzo[e]indoline- and benzothiazoline-derivatives, there is lower steric and electronic bulk, which would lower the rotational barrier around this bond, promoting non-radiative decay mechanisms, and thus no fluorescence (or extremely short-lived). Thus, we rationalised that environmentally induced aggregation may lead to a 'turn-on' in fluorescence, and thus sought to probe this behaviour through analysis of aggregation-induced-emission (AIE).

To investigate the potential AIEgen nature of **3** and **4**, we first sought to analyse the effect of water content in solutions (0%–98% H_2O: THF) of **3** and **4** on AIE behaviours under 440 nm irradiation. As an example, when solutions of aqueous THF ('good solvent') containing **3** (20 μM) were prepared, modifying the water ('poor solvent') fraction (f_w) (0%–98% H_2O) gave a clear increase in f_w (critical f_w of 50%), which is 'switched-off' at higher H_2O concentrations. To probe this phenomenon further we utilised

spectroscopic means, again looking at the effect of f_w on AIE. Compounds **3** and **4** were dissolved to a concentration of 20 μM in aqueous solutions of THF, altering the f_w from 0% to 98% H_2O, and emission spectra were obtained upon each 10% f_w increase. The data was plotted to illustrate the effect of f_w on AIE (Figure 1). In the case of **3**, there is a dramatic increase in observable fluorescence upon an increase of f_w in aqueous THF, where past 60% H_2O there is an appreciable emission maximum observed at 602 nm, with an emission shoulder centred around 650 nm. This emission increased further as f_w increased before quenching can be observed above 90% H_2O. **4** also exhibited similar AIE behaviour when f_w was increased in 20 μM aqueous THF mixtures. There was an observable 'switch-on' of fluorescence from **4** when f_w was increased to 50%, with maximal emission observed at a f_w of 60%, centred around 605 nm, with a secondary emission shoulder at 665 nm. Past a f_w of 60% emission decreased until complete quenching occurred past 80% H_2O in THF. Each of these results are highly indicative of AIE behaviours, as this increase of poor solvent promotes aggregation in these highly conjugated systems, and causes a 'switch-on' in fluorescence. This phenomenon is observable to the naked eye and shows high congruency with spectroscopic analysis. Furthermore, we believe this observation constitutes the first example of an anionophore, with an 'in-built' AIEgen property within the central binding unit.

2.3 | Anion Binding and Transport Studies

To ascertain the strength of association complexes with Cl^- for **1**–**6** we carried out ^1H NMR titrations, in the presence of increasing equivalents of Cl^-. To do this, each compound was dissolved to a concentration of 2.5 mM and ^1H NMR spectra were obtained with each addition of 1 molar equivalent of TBACl. Changes in chemical shift were plotted against anion concentration, and fit to a 1:1 binding mode using *Bindfit* [32], to resolve the association constant for each against Cl^-. These results are summarised below in Table 2.

TABLE 2 | Summary of the lipophilicity, Hammett constants [33] of the aniline substituents and association constants for each compound under study towards Cl^-, as determined through ^1H NMR titrations (DMSO-d_6 (99.5%)/H_2O (0.5%). Binding constants are derived from representative, reproducible titrations; all experiments were repeated to ensure consistency.

Compound	K_a, M^{-1}, (Cl^-)	Error of fit, %	Hammett constant, s [21]	cLogP
1	53	±3.1	+0.86	5.43
2	65	±1.3	+0.54	4.45
3	75	±1.3	+0.86	5.39
4	29	±2.3	+0.54	4.36
5	85	±0.6	+0.86	6.63
6	58	+1.5	+0.54	5.61
7[a]	201	—	+0.86	5.80
8[a]	63	—	+0.54	4.74

[a]Data taken from Ref. [16]. cLogP values were calculated using SwissADME [34].

Taking compound **5** as an example, upon each addition of 1 eq. of Cl^- there is a considerable downfield shift of NH and olefinic CH protons, with minor contributions from *ortho*-aryl and *N*-ethyl CH_2 protons. Fitting this change gave rise to a $K_a = 85\ M^{-1}$, with an error = 0.6% indicating a high accuracy of fit. Compared to that of **7** (201 M^{-1} vs. 85 M^{-1}) we see a decrease in the association constant towards Cl^-. Indeed, when surveying the association constants of each compound under study, we see a markedly low association towards Cl^- across the series under the conditions studied. This is likely due to the electronic density of each heterocycle, which effects the acidity of both squaramide NH, and olefinic CH's, decreasing the binding affinity when compared to **7**. However, it is of note that each receptor displays affinity reminiscent of **8**, which still acts as a potent anionophore in model systems.

Thus, we sought to ascertain the anionophoric ability of receptors **1**–**6** using methods established by Gale and co-workers [35]. We have also seen previously that diminished anion transport in LUV's is not the sole arbitrator of antimicrobial activity for similar agents. We assume that each compound transports via mechanisms similar to **7** and **8**, and as such sought to verify anionophorism in a similar manner as previously demonstrated [28].

Unilamellar vesicles were synthesised using a 7:3 molar ratio of 1-palmitoyl-2-oleoyl-*sn*-glycero-3-phosphocholine (POPC), and cholesterol, containing an internal solution of NaCl (487 mM), which was buffered to pH 7.2, using sodium phosphate buffer (5 mM). Dialysis was utilised to exchange excess external NaCl from vesicles with an isotonic external solution of $NaNO_3$. Using said external solution, the vesicles were brought to a concentration of 0.5 mM before each experiment. The facilitated efflux of Cl^- was monitored through the use of a chloride ion selective electrode (ISE). The anionophoric ability of each compound was monitored at pH 7.2, at a concentration of 5 mol% respective to that of POPC, and were each repeated in triplicate. Receptors were added at 0 s, and addition signified experimental start point. Experimental end point was affected by addition of a Triton X-100 solution (11% *w*/*w* in H_2O:DMSO, 7:1 *v*:*v*) at 300 s, which allowed for calibration to the respective 100% efflux value. The results obtained from these assays are represented graphically in Figure 2.

Anion transport assays indicated that there are key structural facets influencing anion transport in these heterocyclic systems. Much like previously reported indoline counterparts (**7** and **8**), **5** and **6** show high levels of transport efficacy at 5 mol% reaching approximately 95% efflux at the experimental endpoint (300 s). Interestingly, **1**–**4** showed very little transport efficacy regardless of functionalisation, likely due to lower lipophilicity. Among the compounds studied, compound **5** displayed the highest calculated logP value (6.63), which may go some way towards explaining its enhanced transport activity relative to the less lipophilic analogues. Nevertheless, while there have been studies regarding the guided design of anionophores [24], there are several facets which make this hard to predict in a rational manner. These initial experiments indicate that benzo[e]indolyl derivatives may indeed be as effective, as **7** and **8**, however, detailed mechanistic anion transport studies (e.g., transport mode and transporter coupling behaviour) are currently underway in our lab to fully ascertain their anionophoric behaviour. With the knowledge that each compound shows anion transport in LUV's, we

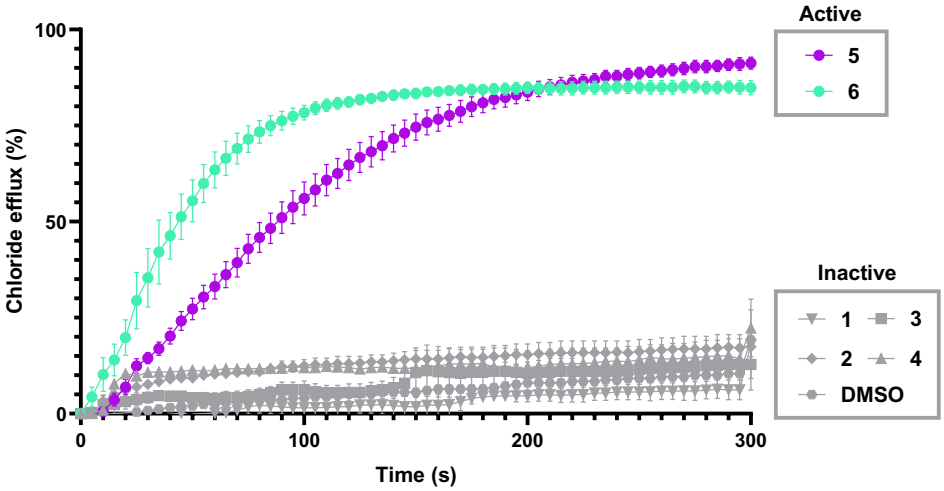

FIGURE 2 | Results of anion transport assay carried out at 5 mol% with respect to lipid, showing transport behaviour for each compound tested. Each compound was added to the solution at $T = 0$ with each receptor being added as a stock solution in DMSO, where addition of DMSO (12 μL) alone was used as control. Experimental end point was determined by the addition of a 11% w/v solution of Triton X-100 in DMSO/H_2O and the obtained 100% efflux was used to determine efflux efficiency of the compounds tested. Data presented is the mean ± SEM of three independent replicates.

next wished to ascertain whether this anion transporting effect manifests in biological activity.

2.4 | Determination of Antimicrobial Effect

To understand the effect of heterocycle upon the biological activity of compounds **1**–**6**, we determined the growth inhibitory ability of each compound against MRSA (clinical isolate, St. James' Hospital, Dublin), and compared it to that of **7**. Growth inhibition assays were carried out using a broth microdilution approach with each compound (200–0.78 μM) against MRSA to determine minimum inhibitory concentration (MIC) (μM) values for each. MIC_{50} values are intended to provide a comparative assessment of antibacterial effects within this new compound series and are defined as the lowest concentration of receptor that resulted in at least 50% inhibition of bacterial growth compared to the untreated control (DMSO). Following treatment and incubation for a 24 h period, each compound was observed to appreciably inhibit MRSA growth, however, when compared to **7**—these compounds perform to a similar degree (**5** and **6**), or less effectively (**1**–**4**) than our previous lead compound.

When comparing MIC_{50} values for each (Table 3), **1** and **2** are less effective than **7**, where the incorporation of a sulphur atom into the heterocycle in place of $C(CH_3)_2$, appears to almost entirely attenuate activity. With MIC_{50} values ≥ 200 μM, these compounds can be deemed therapeutically irrelevant when compared to **7**, as they exhibit a 79- to 59-fold decrease in activity against MRSA. Despite showing lower transport capacity, and lower binding affinity towards Cl^-, **3** and **4** exhibit greater antimicrobial capacity than **1** and **2**. Compounds **3** and **4** have calculated MIC_{50} values ranging from 9.4 (**3**) to 7.5 μM (**4**), which constitute a marked increase in activity as there is only a 2.76- to 2-fold decrease in activity when compared to **7**. However, these results do not exhibit the expected 'dose-response' for antimicrobial agents and as a result we also do not consider these compounds to be analogues worthy of pursuit as antimicrobials. The final two compounds tested, **5** and **6**, showed an increased level of activity against MRSA when compared to **7**, with MIC_{50} concentrations of 1.2 and 2.4 μM, respectively. These MIC_{50} concentrations represent a 0.52- (**5**) and 0.04-fold (**6**) increase in activity, which is an encouraging result that we hypothesise is due to the added planarity bolstering the lipid partitioning ability of these compounds, when compared to **7**. As **5** exhibited both the most potent anion transport (at 5 mol%) and the most potent growth inhibition, we sought to ascertain if there was a link between the two. To verify if this transport behaviour translates to a biological system, we utilised MQAE assays to monitor the in-cellulo Cl^- transport capacity of each compound under study, as previously described by Ko and co-workers [16]. Briefly, cultures brought to early stationary phase were pre-treated with *N*-(ethoxycarbonylmethyl)-6-methoxyquinolinium bromide (MQAE), which acts as a fluorescent probe for intracellular Cl^- concentration. Subsequently, bacteria were treated with a concentration range (25–200 μM) of each compound, whereafter 5 min fluorescence intensity was recorded. The results were plotted as a percentage fluorescence relative to control, and fit to the

TABLE 3 | Results of growth inhibition assays, and the respective MIC_{50} concentration for each compound tested against MRSA. Increase in cytosolic Cl^- concentration induced by treatment of MRSA with Compounds 1–6, at 200 μM for 5 min, quantified by fitting the change in MQAE fluorescence to the Stern–Volmer equation (K_{sv} $Cl^- = 200\ M^{-1}$).

Compound	MRSA MIC_{50}, μM	Quenching efficiency, %	Increase in $[Cl^-]$, mM
1	200	68%	10.4 (±2.4)
2	>200	80%	19.8 (±2.8)
3	9.4	67%	10.1 (±0.5)
4	7.5	75%	14.7 (±0.7)
5	1.2	85%	27.8 (±0.4)
6	2.4	81%	21.2 (±0.6)
7[a]	2.35	—	—

[a]Data taken from Ref. [16].

Stern-Volmer equation to quantify the change in cytosolic Cl^- concentration (Figure 3). The results obtained following fitting are tabulated below in Table 3.

Despite the limited Cl^- transport behaviour in model lipid experiments, each compound under study shows the capacity to increase Cl^- concentration in-cellulo. This result is interesting, as we have previously seen that there is a limited link between model lipid systems, and transport behaviours in-cellulo, and this is further exemplified by this experiment. Despite the observed 10%–15% Cl^- efflux observed for **3** and **4**, in model lipids, we see here a clear concentration dependent decrease in MQAE fluorescence, indicating Cl^- influx. Furthermore, compounds **2**, **5** and **6** generated similar intracellular MQAE quenching signals, yet only **5** and **6** exhibited measurable antimicrobial activity. This result suggests that while the ability to mediate chloride influx is important for antimicrobial activity, it is not on its own sufficient to elicit a biological effect. The disparity between these compounds likely reflects differences in cellular uptake and membrane retention. For example, compound **6**, being more planar and lipophilic, is likely to partition more effectively into and remain associated with the bacterial membrane and potentially sustaining ion transport over the timescale of the growth inhibition assay. In contrast, compound **2** may aggregate or adsorb at the cell surface, producing a transient chloride flux detectable by MQAE but failing to maintain the prolonged ionic imbalance required to inhibit growth. It is important to note that the chloride influx observed in the MQAE assay is interpreted as qualitative evidence of ion transport activity rather than a quantitative reflection of transport efficiency. Furthermore, factors such as compound aggregation, differential membrane localisation, and the electrochemical potential across the bacterial membrane all influence the apparent rate and extent of chloride influx. For these reasons, we interpret the observed fluorescence quenching simply as evidence that these compounds can mediate chloride movement across bacterial membranes.

With the inherent fluorescent characteristics of each compound, we also sought to analyse the cellular uptake of each compound and observe if any appreciable compartmentalisation could be seen upon treatment of MRSA. To do this, MRSA treated with Compounds **1**, **3** and **5** at a concentration of 3 μM for 30 min were subsequently imaged by both super resolution, stimulated emission depletion nanoscopy (STED), and diffraction limited confocal scanning microscopy (*d*-LSCM). Utilising both LSCM white light (WL) laser (EL $\lambda_{455/465/495\,nm}$) and STED depletion laser (DL) (EL $\lambda_{455/465/495\,nm}$, DL $\lambda_{775\,nm}$, 30% power) we analysed the alterations to the fluorescence lifetime of Compounds **1**, **3** and **5**, when excited by WL, and also when emission is depleted (DL), using fluorescence lifetime imaging microscopy (FLIM).Obtaining both

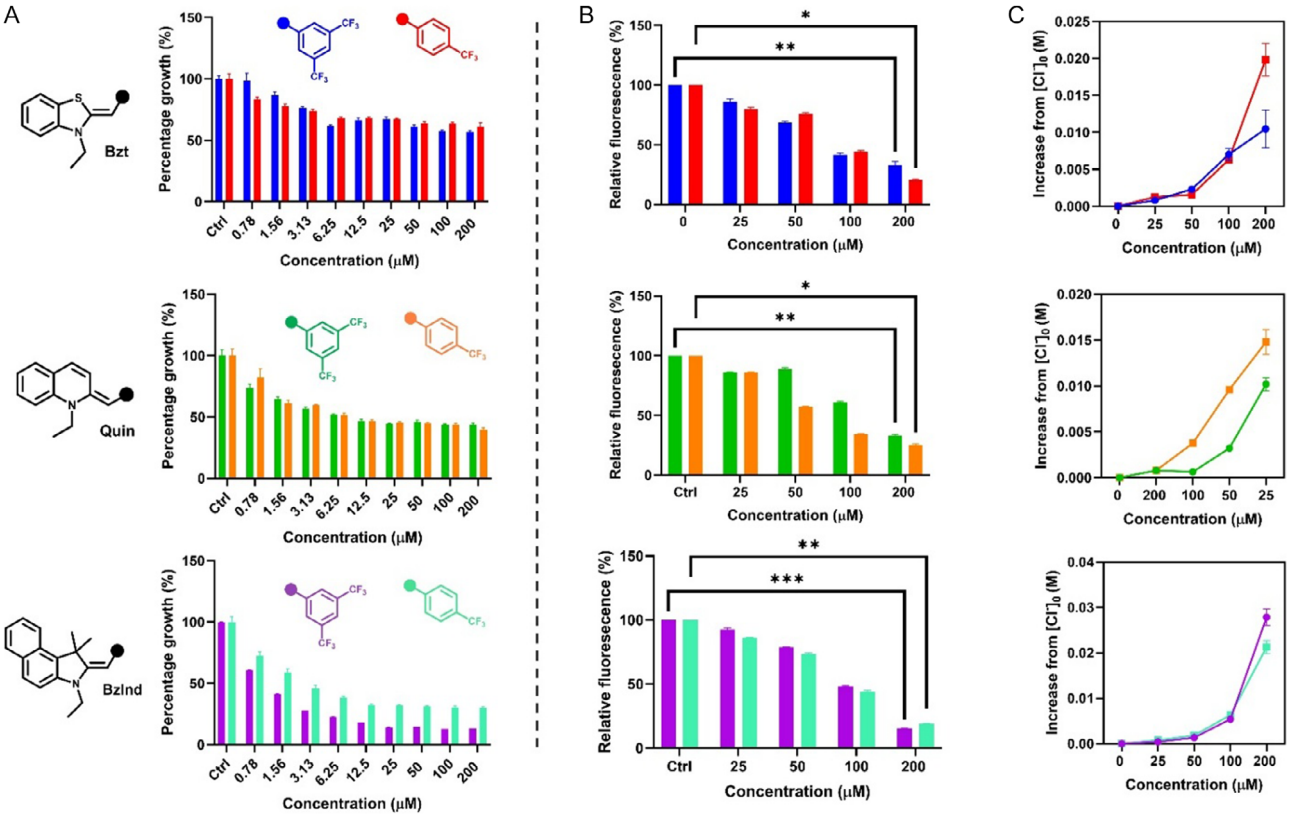

FIGURE 3 | Compounds **1–6** exhibit variable degrees of antimicrobial activity and anion transport capacity in-cellulo. (A) Microbroth dilution assays to determine the bacteriostatic activity of **1–6** against MRSA, represented graphically per heterocyclic substituent. Top = **1–2**, Middle = **3–4**, Bottom = **5–6**. (B) Results of MQAE assays to determine in-cellulo anion transport capacity exhibited by **1–6**. Top = **1–2**, Middle = **3–4**, Bottom = **5–6**. (C) Fitted data of the increase of Cl^- concentration upon treatment with 0–200 μM **1–6**, as determined through the use of MQAE assays. Top = **1–2**, Middle = **3–4**, Bottom = **5–6.** All data represented is the mean (± SEM) of three biological replicates, and represented relative to untreated controls (addition of DMSO carrier to equal concentration (*v*/*v*)) of the highest concentration tested. Statistical comparison was carried out using of two-way ANOVA tests, where * = $p < 0.01$, ** = $p < 0.001$, *** = $p < 0.0001$.

fluorescence lifetime phasor plots and lifetime histograms from both *d*-LSCM and STED depleted images, we were able to demonstrate the STED-ability of each compound (Figure 4).

With this information in hand, that each compound is STED-compatible, we sought to analyse the cellular distribution of each compound using this method. Cells were imaged using CLSM (EL $\lambda_{455/465/495\ nm}$) and STED (EL $\lambda_{455/465/495\ nm}$, DL $\lambda_{775\ nm}$, 30% power, time gating; 0.5–6 ns).

When MRSA was stained with Compound **1**, there is clearly visible, bright green fluorescence centred from cells, that upon analysing the cellular distribution, appears to be largely distributed at the cellular periphery, and not uniformly distributed. Through measurement of fluorescence intensity (Grey values), at both the membrane and within the cytosol of single cells, there is a significantly higher fluorescence localisation ($p > 0.001$) for **1** at the membrane. Furthermore, utilising FLIM, we were able to verify the STEDability of this compound, which is indicated by a shift of the phasor plot towards the right where this shift demonstrates a shortening of the fluorescence lifetime.

In the case of **3**, this lifetime shortening is far more visually apparent from Phasor plots, with a dramatic rightward shift of the major photon incidences again indicating a shortening of the fluorescence lifetime, τ. When analysing the τ histograms, for both LSCM and STED images we see a clear decrease in the lifetime from $t = 7.3$ ns (AIE), to $t = 7.05$ ns. This result is encouraging as not only could we image bacterial cells using STED for this probe, which is now further red-shifted when compared to other compounds tested, we could selectively elucidate the cellular fate of aggregated forms of **3**, using the highly powerful τ-STED mode, through exclusion of photons with shorter lifetimes. Through selective observation of $\tau = 1.5$–11 ns (excimer $\tau = 0.35$ ns), we were able to image cellularly localised AIEgens in MRSA, and able to analyse their cellular compartmentalisation. In this case, AIE forms of **3** appear to be in their majority at the cellular periphery, or membrane localised, through plotting fluorescence intensity from single cells at both the membrane and within the cytosol ($P < 0.0001$). We hypothesise that this membrane localisation permits aggregation of these compounds at the lipid:aqueous interface, as a result of the increased localised concentration in this region. As a result, fluorescence intensity from this region is far in excess of the cytosol, and indeed the extracellular region.

When MRSA was treated with **5** there was a clearly appreciable fluorescent signal localised to cells, that could again be investigated at the single cell level using STED nanoscopy. To first verify the STEDability of **5**, FLIM measurements of τ were carried out using both LSCM, and STED modes, and the resultant phasor plots could be compared. Comparing phasor plots from LSCM to t-STED there is again, a clearly appreciable rightward movement of photon incidences when depleted. This shortening was quantified, where undepleted lifetimes (LSCM) are $\tau = 2.4$ ns, but upon depletion, lifetime decreases to $\tau = 1.6$ ns. Using STED, we were able to analyse the cellular distribution of **5** across MRSA cells, where through plotting of cytosolic and membrane localised fluorescence it is clear that a less distinct than previous, but still quantifiably greater fluorescence intensity within the membrane ($p < 0.001$), again providing evidence to support this membrane localised activity.

When *S. aureus* was previously treated with elevated concentrations of **7**, we observed a concentration dependent increase in cellular aggregation, brought about by a stress response in the bacteria [28]. This was also observed from LFQ proteomic analysis, that self-aggregation was a result of treatment with **7**, and thus we sought to determine if **5** could exert a similar behaviour on MRSA at increased concentrations.

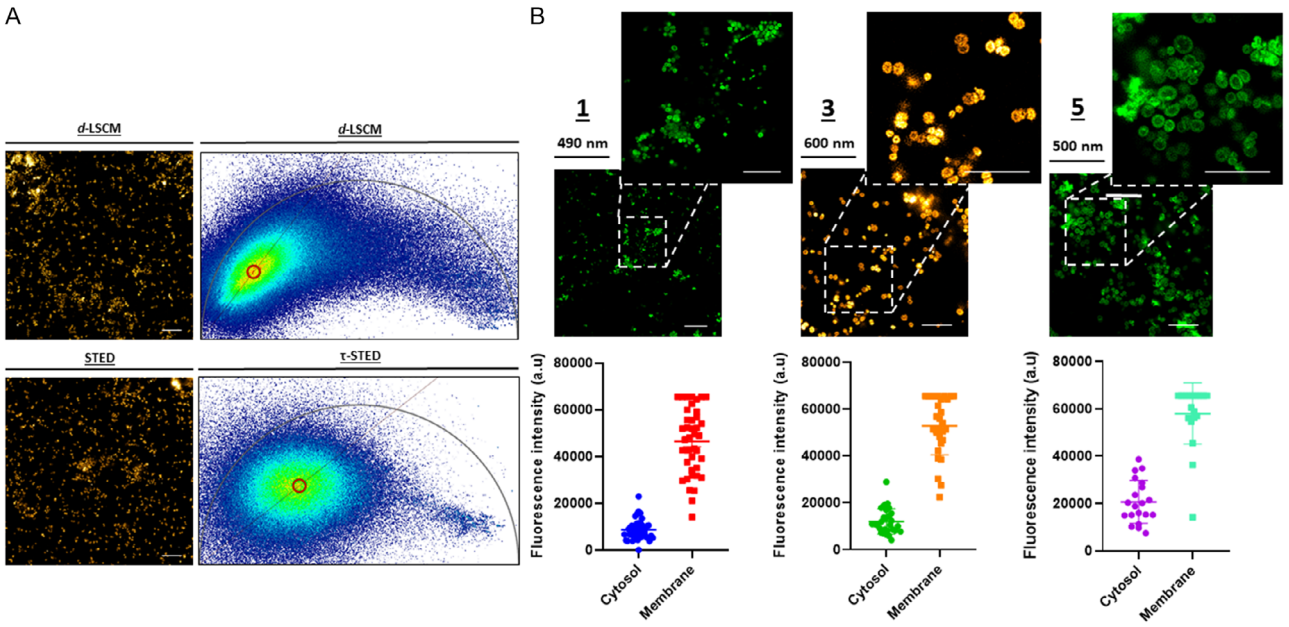

FIGURE 4 | d-LSCM and STED nanoscopy analysis of the cellular uptake of **1**, **3** and **5** in MRSA. (A) d-LSCM, and τ-STED nanoscopy images of MRSA stained with 3 μM **1** (left) and the respective phasor plots for fluorescence lifetime obtained through FLIM (right). (B) Single cell STED nanoscopy analysis of the cellular distribution of **1**, **3** and **5** (3 μM) in MRSA. Data shown is represented as the Mean ± SEM of three biological replicates comprising representative measurements from each replicate, and images presented are representative examples obtained during microscopy experiments. Scale bar = 10 μM.

MRSA was treated with **5** as previously discussed, but this time at a concentration of 50 μM, and samples were prepared for imaging. When samples were imaged, and directly compared to treatment with lower concentrations, there was a visual increase in the level of cellular aggregation, brought about by treatment, which was not observed at the lower treatment dose (3 μM; see ESI). Indeed, this degree of aggregation was so pronounced, that we were able to successfully carry out 3D-STED analysis of these aggregates, resulting in the 3D reconstitution of one representative aggregate (see ESI). Showing uniform fluorescence throughout the aggregate, we believe the formation of these aggregates is brought about by a stress response induced by **5**. If aggregation was occurring prior to treatment, we would likely see limited fluorescence from the centre of these aggregates. These observations suggest that these compounds have a high spatial preference for bacterial membranes, and may exert their activity through some membrane active anion transport mechanisms, as previously observed for compound **7**. However, while our data collectively supports a link between anion transport and antimicrobial activity, it should be noted that these experiments do not definitively exclude a contribution from cation transport or broader membrane-disruptive effects. The current work therefore demonstrates correlation rather than exclusivity, and further mechanistic studies such as Na^+-selective electrode assays or ion-pair transport analyses will be required to fully deconvolute the MOA.

3 | Conclusion

A series of novel squaramide constructs containing both a variety of *N*-heterocycles, and poly fluorinated anilines have been synthesised, through a modular approach. These novel motifs show modest levels of anion binding in DMSO-d_6. With varying degrees of anion transport behaviour in model lipid vesicles, we sought to ascertain the in-cellulo correlation of anion transport, where each compound shows greater transport capacity when studied in bacterial cells. This in-cellulo anion transport manifests in variable antimicrobial activity across the series. By comparing previous observations of related compounds, we suggest that the antimicrobial activity is likely linked to both membrane localisation and anion transport. To study this, we utilised STED nanoscopy as a tool to profile the cellular distribution of **1**–**6.** Each shows bright fluorescence, within single MRSA cells, where it was observed a high level of membrane localisation for each. This imaging confirms that the compounds localise to the bacterial membrane, and, in the context of the transport assays and the MQAE assay data, also supports the hypothesis that these compounds may function as membrane-active anion transporters. While the present study does not establish anion transport as the sole determinant of antimicrobial activity, the collective results indicate that membrane localisation and chloride transport act in concert to perturb bacterial ion homeostasis, thereby contributing to the observed biological effects. We believe that this work further advances knowledge of supramolecular approaches to antimicrobial development and work is currently ongoing in our lab to further investigate more effective routes to optimise lead compounds, generate design rules for the development of antimicrobial anionophores and evaluate transport behaviour in membrane systems that more closely mimic bacterial lipid compositions, with the aim of refining design principles for antimicrobial anionophores.

4 | Statistical Analysis

All data presented was analysed using Graphpad Prism 9.0.1 and is presented as the mean ± SEM of each dataset, comprising three independent replicates ($n = 3$) for biological experiments. Where necessary, data transformation and normalisation were carried out to enhance clarity of the results utilising in-built tools in Prism. Statistical tests utilised were either one- or two-way ANOVA tests, and statistical significance was determined as $p > 0.01$.

Author Contributions

Robert Brian Peter Elmes, **Kevin Kavanagh**, and **Luke Edward Brennan** designed the study and wrote the manuscript. **Robert Brian Peter Elmes** and **Kevin Kavanagh** supervised the study. **Luke Edward Brennan** synthesised the compounds under study, carried out photophysical and spectroscopic analysis, performed all biological evaluation, and all statistical analyses. **Chris Samuel Hawes** performed single crystal X-ray crystallography. All authors discussed the results and commented on the manuscript.

Acknowledgements

L. E. B. thanks the Irish Research Council (IRC) for a Government of Ireland Postgraduate Scholarship (GOIPG/2020/78), and RCSI (Prof. Donal O'Shea, Department of Chemistry) for access to the Super Resolution Imaging Consortium. R. B. P. E. and K. K. acknowledge funding from Science Foundation Ireland (SFI) (Grant no. 12/RC/2275/P2), which is cofunded under the European Regional Development Fund. SFI is also acknowledged for funding of the NMR facility (12/RI/2346/SOF) through the Research Infrastructure Programme. Dr. Massimiliano Garre is thanked for his insight regarding STED analysis of microbial samples.

Funding

This study was supported by Science Foundation Ireland (12/RC/2275/P2, 12/RI/2346/SOF, 18/RI/5723), Irish Research Council for Science, Engineering and Technology (GOIPG/2020/78).

Conflicts of Interest

The authors declare no conflicts of interest.

Data Availability Statement

The data that support the findings of this study are available in the supplementary material of this article.

References

1. L. J. Piddock, "The Crisis of No New Antibiotics-What Is the Way Forward?," *Lancet Infectious Diseases* 12, no. 3 (2012): 249–253, https://doi.org/10.1016/s1473-3099(11)70316-4.

2. C. J. L. Murray, K. S. Ikuta, F. Sharara, et al., "Global Burden of Bacterial Antimicrobial Resistance in 2019: A Systematic Analysis," *Lancet* 399, no. 10325 (2022): 629–655, https://doi.org/10.1016/S0140-6736(21)02724-0, (acccessed 2024/01/03).

3. P. M. Hawkey, "The Origins and Molecular Basis of Antibiotic Resistance," *Bmj* 317, no. 7159 (1998): 657–660, https://doi.org/10.1136/bmj.317.7159.657.

4. M. J. and L. Amaral, "Mechanisms of Drug Efflux and Strategies to Combat Them: Challenging the Efflux Pump of Gram-Negative Bacteria," *Biochimica et Biophysica Acta* 1794, no. 5 (2009): 826–833, https://doi.org/10.1016/j.bbapap.2008.12.011.

5. S. Santajit and N. Indrawattana, "Mechanisms of Antimicrobial Resistance in ESKAPE Pathogens," *Biomed Research International* 2016 (2016): 2475067, https://doi.org/10.1155/2016/2475067.

6. J. M. Munita and C. A. Arias, "Mechanisms of Antibiotic Resistance," *Microbiology Spectroscopy* 4, no. 2 (2016): 1–24 https://doi.org/10.1128/microbiolspec.VMBF-0016-2015.

7. K. M. Overbye and J. F. Barrett, "Antibiotics: where Did We Go Wrong?," *Drug Discovery Today* 10, no. 1 (2005): 45–52, https://doi.org/10.1016/s1359-6446(04)03285-4.

8. M. I. Hutchings, A. W. Truman, and B. Wilkinson, "Antibiotics: Past, Present and Future," *Current Opinion in Microbiology* 51 (2019): 72–80, https://doi.org/10.1016/j.mib.2019.10.008.

9. J.-M. Lehn, "Supramolecular Chemistry—Scope and Perspectives Molecules, Supermolecules, and Molecular Devices (Nobel Lecture)," *Angewandte Chemie International Edition in English* 27, no. 1 (1988): 89–112, https://doi.org/10.1002/anie.198800891.

10. C. J. Pedersen, "The Discovery of Crown Ethers (Noble Lecture),"*Angewandte Chemie International Edition in English* 27, no. 8 (1988): 1021–1027, https://doi.org/10.1002/anie.198810211.

11. D. J. Cram, "The Design of Molecular Hosts, Guests, and Their Complexes (Nobel Lecture," *Angewandte Chemie International Edition in English* 27, no. 8 (1988): 1009–1020, https://doi.org/10.1002/anie.198810093.

12. N. Busschaert, C. Caltagirone, W. Van Rossom, and P. A. Gale, "Applications of Supramolecular Anion Recognition," *Chemical Reviews* 115, no. 15 (2015): 8038–8155, https://doi.org/10.1021/acs.chemrev.5b00099.

13. N. H. Evans and P. D. Beer, "Advances in Anion Supramolecular Chemistry: From Recognition to Chemical Applications," *Angewandte Chemie International Edition* 53, no. 44 (2014): 11716–11754, https://doi.org/10.1002/anie.201309937.

14. J. T. Davis, P. A. Gale, and R. Quesada, "Advances in Anion Transport and Supramolecular Medicinal Chemistry," *Chemical Society Reviews* 49, no. 16 (2020): 6056–6086, https://doi.org/10.1039/C9CS00662A.

15. A. Gianotti, V. Capurro, L. Delpiano, et al., "Small Molecule Anion Carriers Correct Abnormal Airway Surface Liquid Properties in Cystic Fibrosis Airway Epithelia," *International Journal of Molecular Sciences* 21, no. 4 (2020): 1488, https://doi.org/10.3390/ijms21041488.

16. S. K. Ko, S. K. Kim, A. Share, et al., "Synthetic Ion Transporters Can Induce Apoptosis by Facilitating Chloride Anion Transport into Cells," *Nature Chemistry* 6, no. 10 (2014): 885–892, https://doi.org/10.1038/nchem.2021.

17. L. A. Marchetti, L. K. Kumawat, N. Mao, J. C. Stephens, and R. B. P. Elmes, "The Versatility of Squaramides: From Supramolecular Chemistry to Chemical Biology," *Chem* 5, no. 6 (2019): 1398–1485, https://doi.org/10.1016/j.chempr.2019.02.027.

18. P. A. Gale, J. T. Davis, and R. Quesada, "Anion Transport and Supramolecular Medicinal Chemistry," *Chemical Society Reviews* 46, no. 9 (2017): 2497–2519, https://doi.org/10.1039/C7CS00159B.

19. N. Busschaert, S. H. Park, K. H. Baek, et al., "A Synthetic Ion Transporter that Disrupts Autophagy and Induces Apoptosis by Perturbing Cellular Chloride Concentrations," *Nature Chemistry* 9, no. 7 (2017): 667–675, https://doi.org/10.1038/nchem.2706.

20. S. N. Berry, V. Soto-Cerrato, E. N. W. Howe, et al., "Fluorescent Transmembrane Anion Transporters: Shedding Light on Anionophoric Activity in Cells," *Chemical Science* 7, no. 8 (2016): 5069–5077, https://doi.org/10.1039/c6sc01643j.

21. V. Soto-Cerrato, P. Manuel-Manresa, E. Hernando, et al., "Facilitated Anion Transport Induces Hyperpolarization of the Cell Membrane That Triggers Differentiation and Cell Death in Cancer Stem Cells," *Journal of American Chemical Society* 137, no. 50 (2015): 15892–15898, https://doi.org/10.1021/jacs.5b09970.

22. I. Carreira-Barral, C. Rumbo, M. Mielczarek, et al., "Small Molecule Anion Transporters Display In Vitro Antimicrobial Activity against Clinically Relevant Bacterial Strains," *Chemical Communications* 55, no. 68 (2019): 10080–10083, https://doi.org/10.1039/C9CC04304G.

23. C. R. Elie, G. David, and A. R. Schmitzer, "Strong Antibacterial Properties of Anion Transporters: A Result of Depolarization and Weakening of the Bacterial Membrane," *Journal of Medicinal Chemistry* 58, no. 5 (2015): 2358–2366, https://doi.org/10.1021/jm501979f.

24. A. I. Share, K. Patel, C. Nativi, et al., "Chloride Anion Transporters Inhibit Growth of Methicillin-Resistant Staphylococcus Aureus (MRSA) In Vitro," *Chemical Communications* 52, no. 48 (2016): 7560–7563, https://doi.org/10.1039/C6CC03645G.

25. K. Maslowska-Jarzyna, A. Cataldo, A. Marszalik, et al., "Dissecting Transmembrane Bicarbonate Transport by 1,8-Di(thio)amidocarbazoles," *Organic & Biomolecular Chemistry* 20, no. 38 (2022): 7658–7663, https://doi.org/10.1039/D2OB01461K.

26. E. E. Hickey, S. W. Page, and D. J. Trott, "In Vitro Efficacy and Pharmacodynamic Profiles of Four Polyether Ionophores against Methicillin-Resistant Staphylococcus Spp," *Journal of Veterinary Pharmacology and Therapeutics* 43, no. 5 (2020): 499–507, https://doi.org/10.1111/jvp.12871.

27. S. R. Herschede, R. Salam, H. Gneid, and N. Busschaert, "Bacterial Cytological Profiling Identifies Transmembrane Anion Transport as the Mechanism of Action for a Urea-Based Antibiotic," *Supramolecular Chemistry* 34, no. 1 (2022): 26–33, https://doi.org/10.1080/10610278.2023.2178921.

28. L. E. Brennan, L. K. Kumawat, M. E. Piatek, et al., "Potent Antimicrobial Effect Induced by Disruption of Chloride Homeostasis," *Chem* 9, no. 11 (2023): 3138–3158, https://doi.org/10.1016/j.chempr.2023.07.014, (acccessed 2025/01/17).

29. L. E. Brennan, X. Luo, F. A. Mohammed, K. Kavanagh, and R. B. P. Elmes, "Uncovering the Potent Antimicrobial Activity of Squaramide Based Anionophores – Chloride Transport and Membrane Disruption," *Chemical Science* 16, no. 9 (2025): 4075–4084, https://doi.org/10.1039/D4SC01693A.

30. L. A. Marchetti, T. Krämer, and R. B. P. Elmes, "Amidosquaramides – a New Anion Binding Motif with pH Sensitive Anion Transport Properties," *Organic & Biomolecular Chemistry* 20, no. 35 (2022): 7056–7066, https://doi.org/10.1039/D2OB01176J.

31. K. T. Mahmudov, A. V. Gurbanov, V. A. Aliyeva, M. F. C. Guedes da Silva, G. Resnati, and A. J. L. Pombeiro, "Chalcogen Bonding in Coordination Chemistry," *Coordination Chemistry Reviews* 464 (2022): 214556, https://doi.org/10.1016/j.ccr.2022.214556.

32. D. B. Hibbert and P. Thordarson, "The Death of the Job Plot, Transparency, Open Science and Online Tools, Uncertainty Estimation Methods and Other Developments in Supramolecular Chemistry Data Analysis," *Chemical Communications* 52, no. 87 (2016): 12792–12805, https://doi.org/10.1039/C6CC03888C.

33. D. H. McDaniel and H. C. Brown, "An Extended Table of Hammett Substitutent Constants Based on the Ionization of Substituted Benzoic Acids," *The Journal of Organic Chemistry* 23, no. 3 (1958): 420–427, https://doi.org/10.1021/jo01097a026.

34. A. Daina, O. Michielin, and V. Zoete, "SwissADME: A Free Web Tool to Evaluate Pharmacokinetics, Drug-Likeness and Medicinal Chemistry Friendliness of Small Molecules," *Scientific Reports* 7, no. 1 (2017): 42717, https://doi.org/10.1038/srep42717.

35. L. A. Jowett and P. A. Gale, "Supramolecular Methods: The Chloride/Nitrate Transmembrane Exchange Assay," *Supramolecular Chemistry* 31, no. 5 (2019): 297–312, https://doi.org/10.1080/10610278.2019.1574017.

36. N. Busschaert, S. J. Bradberry, M. Wenzel, et al., "Towards Predictable Transmembrane Transport: QSAR Analysis of Anion Binding and Transport," *Chemical Science* 4, no. 8 (2013): 3036–3045, https://doi.org/10.1039/C3SC51023A.

37. M. E. M. Mekhzoum, E. M. Essassi, A. Qaiss, and R. Bouhfid, "Fluorescent Bio-Nanocomposites Based on Chitosan Reinforced Hemicyanine Dye-Modified Montmorillonite," *RSC Advances* 6, no. 112 (2016): 111472–111481, https://doi.org/10.1039/C6RA23320A.

38. T. Hirata, H. Kogiso, K. Morimoto, et al., "Synthesis and Reactivities of 3-Indocyanine-Green-Acyl-1,3-Thiazolidine-2-Thione (ICG-ATT) as a New Near-Infrared Fluorescent-Labeling Reagent," *Bioorganic & Medicinal Chemistry* 6, no. 11 (1998): 2179–2184, https://doi.org/10.1016/S0968-0896(98)00156-4.

Supporting Information

Additional supporting information can be found online in the Supporting Information section. All datasets and experimental procedures supporting this article have been uploaded as part of the ESI. The authors have cited additional references within the Supporting Information [36–38]. **Supporting Fig. S1:** ^{1}H NMR stackplot, 5.0–13.0 ppm, of receptor **1** with 0.0–22.0 equivalents of TBACl in DMSO-d_6/0.5% H_2O. **Supporting Fig. S2:** Fitted binding isotherm for the titration of **1** (2.5×10^{-6} M) in the presence of increasing concentrations of Cl^- in DMSO-d_6/0.5% H_2O. The data is fitted to a 1:1 binding model and shows the chemical shift of the NH signals throughout the titration. Ka = 53 M^{-1}, Error = 3.08%. http://app.supramolecular.org/bindfit/view/466f78bd-4e6a-4a17-ac98-ee4785242dd5. **Supporting Fig. S3:** Residuals plot of **1**. **Supporting Fig. S4:** ^{1}H NMR stackplot, 3.8–12.5 ppm, of receptor **2** with 0.0–22.0 equivalents of TBACl in DMSO-d_6/0.5% H_2O. **Supporting Fig. S5:** Fitted binding isotherm for the titration of 2 (2.5×10^{-6} M) in the presence of increasing concentrations of Cl^- in DMSO-d_6/0.5% H_2O. The data is fitted to a 1:1 binding model and shows the chemical shift of the NH signals throughout the titration. Ka = 65 M^{-1}, Error = 1.25%. http://app.supramolecular.org/bindfit/view/be5df785-016f-4233-ba60-3e18f307393d. **Supporting Fig. S6:** Residual plot of **2**. **Supporting Fig. S7:** ^{1}H NMR stackplot, 4.0–15.5 ppm, of receptor **3** with 0.0–22.0 equivalents of TBACl in DMSO-d_6/0.5% H_2O. **Supporting Fig. S8:** Fitted binding isotherm for the titration of **3** (2.5×10^{-6} M) in the presence of increasing concentrations of Cl– in DMSO-d_6/0.5% H_2O. The data is fitted to a 1:1 binding model and shows the chemical shift of the NH signals throughout the titration. Ka = 75.03 M^{-1}, Error = +1.29%. http://app.supramolecular.org/bindfit/view/bbcb93ea-7901-4003-9ceee00e2792fe39. **Supporting Fig. S9:** Residual plot of **3**. **Supporting Fig. S10:** ^{1}H NMR stackplot, 4.0–13.0 ppm, of receptor **4** with 0.0–22.0 equivalents of TBACl in DMSO-d_6/0.5% H_2O. **Supporting Fig. S11:** Fitted binding isotherm for the titration of **4** (2.5×10^{-6} M) in the presence of increasing concentrations of Cl^- in DMSO-d_6/0.5% H_2O. The data is fitted to a 1:1 binding model and shows the chemical shift of the NH signals throughout the titration. Ka = 29 M^{-1}, Error = +2.3%. http://app.supramolecular.org/bindfit/view/f8e1e305-102f-407d-8919-149580259280. **Supporting Fig. S12:** Residual plot of **4**. **Supporting Fig. S13:** ^{1}H NMR stackplot, 4.0–13.0 ppm, of receptor **5** with 0.0–22.0 equivalents of TBACl in DMSO-d_6/0.5% H_2O. **Supporting Fig. S14:** Fitted binding isotherm for the titration of **5** (2.5×10^{-6} M) in the presence of increasing concentrations of Cl^- in DMSO-d_6/0.5% H_2O. The data is fitted to a 1:1 binding model and shows the chemical shift of the NH signals throughout the titration. Ka = 48.66 M^{-1}, Error = +1.5%. http://app.supramolecular.org/bindfit/view/e25942de-c95b-4545-93d4-2b2d894911af. **Supporting Fig. S15:** Residual plot of **5**. **Supporting Fig. S16:** ^{1}H NMR stackplot, 4.0–12.5 ppm, of receptor **6** with 0.0–22.0 equivalents of TBACl in DMSO-d_6/0.5% H_2O. **Supporting Fig. S17:** Fitted binding isotherm for the titration of **6** (2.5×10^{-6} M) in the presence of increasing concentrations of Cl^- in DMSO-d_6/0.5% H_2O. The data is fitted to a 1:1 binding model and shows the chemical shift of the NH signals throughout the titration. Ka = 85 M^{-1}, Error = +0.58%. http://app.supramolecular.org/bindfit/view/51217a46-1d38-489e-b42f-1455eb09ed3f. **Supporting Fig. S18:** Residual plot of **6**. **Supporting Fig. S19:** Normalised UV-vis/emission spectrum of **1**. **Supporting Fig. S20:** Normalised UV-vis/emission spectrum of **2**. **Supporting Fig. S21:** Normalised UV-vis/emission spectrum of **5**. **Supporting Fig. S22:** Normalised UV-vis/emission spectrum of **6**. **Supporting Fig. S23:** 3D reconstitution of a representative MRSA cellular aggregate, imaged using 3D-STED, from a series of Zstack images. Images were deconvoluted, and stitched to comprise the 3D render using the Leica LasX software. **Supporting Fig. S24:** X-ray crystal structure of Compound **1**, obtained as a DMSO solvate. Left indicates the molecular structure andDMSO binding mode through both CH and NH motifs. Right indicates the π–π stacking behaviour of compound **1** in the solid state. **Supporting Table 1:** Crystal and refinement parameters for all structures.